Osmium-isotope evidence for volcanism across the Wuchiapingian–Changhsingian boundary interval

Zeyang Liu[a]*, David Selby[a,e], Hua Zhang[b], Quanfeng Zheng[b], Shuzhong Shen[c], Bradley B. Sageman[d], Stephen E. Grasby[f,g], Benoit Beauchamp[g]

[a]Department of Earth Sciences, Durham University, Durham DH1 3LE, UK

[b]State Key Laboratory of Palaeobiology and Stratigraphy, Nanjing Institute of Geology and Palaeontology and Center for Excellence in Life and Paleoenvironment, Chinese Academy of Sciences, 39 East Beijing Road, Nanjing 210008, China

[c]School of Earth Sciences and Engineering, Nanjing University, Nanjing, 210023, China

[d]Department of Geological Sciences, Northwestern University, Evanston, IL 60208, USA

[e]State Key Laboratory of Geological Processes and Mineral Resources, School of Earth Resources, China University of Geosciences, Wuhan, 430074, Hubei, China

[f]Geological Survey of Canada, Calgary Natural Resources Canada, 3303 33rd Street NW, Calgary, AB, T2L 2A7, Canada

[g]Department of Geoscience, University of Calgary, 2500 University Drive NW Calgary, AB, T2N 1N4, Canada

[*]Corresponding author: geozy.liu@outlook.com

Abstract:

Two negative carbon isotope excursions (3.5–6.5‰) across the Wuchiapingian-Changhsingian boundary (WCB) are observed globally (sections in China, Canada, and Iran); however, the causative mechanism of these excursions is debated. Here, high-resolution osmium isotope ($^{187}Os/^{188}Os$ or Os_i) chemostratigraphy of four globally correlated WCB sections (3 in China - Meishan, Shangsi and Lianyuan and 1 in Canada - Buchanan Lake) show two separate Os_i excursions to less radiogenic compositions that are coincident with the carbon isotope shifts for two of the South China sections (Lianyuan, Meishan). In contrast, only a single Os_i excursion to less radiogenic compositions, coinciding with the earliest Changhsingian carbon isotope shift, is observed for the Shangsi and Buchanan Lake sections. The Os_i shift is interpreted to reflect increased unradiogenic Os input from basaltic magmatism in South China, possibly related to the Emeishan large igneous province (LIP). However, $^{187}Os/^{188}Os$ data suggest that only the earliest Changhsingian volcanism had global impact on both the ocean and atmosphere. The lack of any evidence for a biotic event associated with the WCB therefore may have been due to the more regional rather than global impact of volcanism during the latest Wuchiapingian. In contrast, during the earliest Changhsingian, volcanism was sufficient to cause a more global signal in the ocean osmium record, but was inadequate, or too prolonged, to drive any significant environmental change. Volcanism, however, may have provided the isotopically light carbon that drove the negative carbon isotope excursions across the WCB.

Keywords: Wuchiapingian–Changhsingian boundary, osmium isotope, volcanism, South China, Canadian Arctic, carbon isotopes

1. Introduction

Carbon isotope excursions (CIEs) temporally coincide with geological and biological crises throughout Earth history, e.g., end-Ordovician, Frasnian–Famennian, end-Permian, end-Triassic and end-Cretaceous mass extinction events (Bond and Grasby, 2017). Although the mechanisms driving CIEs remain debated, some are thought to be caused by the release of isotopically light carbon gas arising either directly or indirectly from the volcanic event. (e.g. collapse of the biological pump, increase in organic-carbon weathering, CO_2 released from Large Igneous Provinces (LIPs), changes in organic carbon burial, etc.: Kump and Arthur, 1999; Payne and Kump, 2007, and references therein). Three CIEs are documented during the Late Permian (Korte and Kozur, 2010) that span the Guadalupian–Lopingian boundary (GLB – ~259 Ma) (Shen et al., 2019b), the Wuchiapingian–Changhsingian boundary (WCB – ~254 Ma) (Shao et al., 2000; Shen et al., 2013), and the Permian–Triassic boundary (PTB – ~252 Ma) (Korte and Kozur, 2010). The latter coincides with the end-Permian mass extinction, which is the largest mass extinction event of the Phanerozoic (Erwin, 2006).

The large negative CIE globally documented by analysis of carbonate ($\delta^{13}C_{carb}$) and organic matter ($\delta^{13}C_{org}$) within the interval immediately below the Permian–Triassic boundary (Korte and Kozur, 2010) is interpreted to be caused by the emission of volcanic CO_2 from widespread volcanism in Siberia and South China (Payne and Kump, 2007; Shen et al., 2013; Shen et al., 2019a; Svenson et al., 2009) and/or associated carbon release from sedimentary strata (Saunders and Reichow, 2009; Shen et al., 2011). Similarly, the negative CIE (1.7–8‰) of the Guadalupian–Lopingian boundary documented at several sections (e.g., South China, Iran, Spitsbergen) (Bond et al., 2015; Jin et al., 2006a; Shen et al., 2013; Wang et al., 2004; Wignall et al., 2009) coincides with the timing of the Emeishan volcanism in South China, which is ultimately linked with the end-Guadalupian mass extinction (Wignall, 2001; Wignall et al., 2009).

In contrast, distinctive negative CIEs across the WCB are not known in all sections, which has been considered to be a reflection of sampling resolution of previous studies (Shen et al., 2013). However, sections that do exhibit two negative CIEs across the WCB interval, although with different patterns, are observed in several sections in South China (Bagherpour et al., 2018; Bai et al., 2008; Jin et al., 2006b; Shao et al., 2000; Shen et al., 2013, 2010; Wei et al., 2015; Ye and Jiang, 2016), Iran (Liu et al., 2013; Shen et al., 2013) and one section in the Canadian Arctic (Beauchamp et al., 2009) (Fig. 1). Unlike the PTB and the GLB, which also have CIEs that are globally recorded, no geological or biological events are linked to the WCB negative CIEs (Shen et al., 2013). Moreover, the driving mechanism of the WCB CIEs have not been linked to volcanism, but in contrast, they have been linked to low primary productivity (Wei et al., 2015) and/or oxidation of exposed organic carbon within peat/coal formations of dry climatic regions (Shao et al., 2000). Other such mechanisms that can cause negative CIEs, for example rapid methane release from the sea floor and / or the heating of organic matter through magma interaction, have been dismissed based on the gradual nature of the negative CIEs across the WCB (Wei et al., 2015).

In this study, we present high-resolution osmium isotope ($^{187}Os/^{188}Os$, Os_i) stratigraphy across the correlative WCB sections of Lianyuan, Meishan and Shangsi in South China, and the Buchanan Lake section in the Canadian Arctic, to examine the relationship between carbon isotope and osmium isotope records as a means to better elucidate the potential cause and global extent of the CIEs. The Os data exhibit two marked nonradiogenic shifts in Os_i that coincide with the carbon isotope perturbations across the WCB interval, but only the Os_i shift within the earliest Changhsingian is represented globally (Fig. 2). The Os_i shifts are interpreted to be a result of short-lived (700 kyrs) Emeishan volcanism (Shellnutt, 2014), which we argue may explain the lack of any global biological crisis across the WCB interval. We consider this volcanism to have been only regional in extent during the Late Wuchiapingian, but generated

90 enough isotopically light carbon to perturb the global carbon isotope signature. Volcanism may
91 have been more extensive during the Early Changhsingian, thus affecting both the global
92 seawater $^{187}Os/^{188}Os$ composition and the carbon cycle.

93 **2. Geology of the studied interval**

94 South China was situated in the eastern part of the Palaeotethys Ocean during the Late
95 Wuchiapingian to Early Changhsingian (Fig. 1). Three sections (Lianyuan, Meishan, Shangsi)
96 spanning the WCB were sampled that record deposition from deltaic and shallow nearshore to
97 progressively more offshore open marine environments, respectively (Li and Shen, 2008;
98 Wang and Jin, 2000). The section from the Canadian Arctic (Buchanan Lake) records
99 deposition on the north-western margin of Pangea during the Late Wuchiapingian to Early
100 Changhsingian (Fig. 1). The section represents deep shelf, and slope to basin environments
101 (Beauchamp et al., 2009; Grasby and Beauchamp, 2008). Correlations between the sections are
102 based on high-resolution carbon isotope records, conodont biozones, CA-TIMS U-Pb zircon
103 ages and the Os_i data from this study (Fig. 2).

104 **2.1 Lianyuan**

105 The most proximal depositional setting is represented by the Lianyuan locality in the
106 Hunan Province (27.8911° N;111.8618° E), where both the Upper Lungtan and Lower Talung
107 Formations record the WCB interval in a fresh road-cut. The formations record a transgressive
108 depositional sequence from a deltaic environment to an open marine basin setting across the
109 WCB interval (Li and Shen, 2008; Wang and Jin, 2000). The Lungtan Formation comprises
110 black silty sandstone, which gradually transitions into the Talung Formation, itself
111 characterized by interbedded shale/mudstone with a ~30 cm coal bed. Overlying the coal bed,
112 the Talung Formation is mainly composed of marine facies including black shale/mudstone,
113 siliceous mudstone, calcareous mudstone and chert. The Upper Lungtan Formation contains
114 brachiopods (*Tyloplecta yangtzeensis*, *Permophricodothyris grandis*, *Haydenella kiangsiensis*)

and bivalves (*Schizodus pinguis*, *S. guizhouensis*, *Gujocardita cura*) that only constrain the timing of deposition to Wuchiapingian or Changhsingian. Fossil flora (*Gigantopteris nicotianaefolia-Lobatannularia multifolia* Zone) suggests a similar age range. However, the first occurrence of the conodont *Clarkina wangi* occurs in the lower part of the Talung Formation (Ye and Jiang, 2016). Based on this, the WCB is placed within the Lower Talung Formation, as noted for the Shangsi Section, permitting correlation with the Meishan and Shangsi sections of South China (Fig. 2; Jin et al., 2006b; Shen et al., 2013; Yuan et al., 2019).

2.2 Meishan

The Meishan section in Changxing County, hosts the Global Stratotype Section and Point (GSSP) for the Wuchiapingian-Changhsingian boundary (Jin et al., 2006b). It represents a transition from a shallow marine, possibly dysoxic (organic-rich) environment in the upper part of the Lungtan Formation to a slope carbonate setting across the WCB. The Lungtan Formation is predominantly characterized by silty sandstone, mudstone, and shale, and contains abundant brachiopods (Li and Shen, 2008). The overlying Changhsing Formation is dominated by limestone with abundant ammonoids and some fusulinids, and is also characterised by multiple ash beds. The basal boundary of the Changhsingian Stage is defined by the first appearance datum (FAD) of *Clarkina wangi* (Jin et al., 2006b). Zircon CA-TIMS U-Pb dating of Beds 6 and 7 (4.9 m and 5.4 m above the FAD of *Clarkina wangi*) yield an age of 253.49 ± 0.07 Ma and 253.45 ± 0.08 Ma, respectively (Shen et al., 2011). The $\delta^{13}C_{carb}$ profile for this interval appears to shift to a more positive baseline in the uppermost part of the Lungtan Formation (Fig. 2), but also exhibits two negative shifts of ~2–3 ‰ that bracket the WCB (Fig. 2; see Results for detail).

2.3 Shangsi

The Shangsi location near Guangyuan, Sichuan Province is an intensively studied Permian section (Riccardi et al., 2007; Shen et al., 2011; Yuan et al., 2019). At Shangsi the

Wuchiaping Formation is composed of organic-rich carbonate, and is overlain by the predominantly siliceous or cherty carbonate of the Talung Formation. The Talung Formation, from the latest Wuchiapingian through the Early Changhsingian, represents the facies with the deepest depositional environment (shelf-slope) of the studied sites. Both formations include beds rich in organic content (total organic carbon, or TOC = 0.87 - 5 wt. %) and contain abundant ammonoids and conodonts (Yuan et al., 2019). Zircon CA-TIMS U-Pb dating from tuff units at 0.9 m below and 3.4 m above the first occurrence of *Clarkina wangi* yield an age of 254.31 ± 0.07 Ma and 253.60 ± 0.08 Ma, respectively (Shen et al., 2011). The $\delta^{13}C_{carb}$ profile differs from Meishan, showing a broad trend toward more negative, and then more positive values (Fig. 2), but also includes possible shorter term negative excursions that bracket the WCB (see "Results" below).

2.4 Buchanan Lake

The Buchanan Lake section is situated in the Sverdrup Basin of the Canadian Arctic (Grasby and Beauchamp, 2008). This section records a transgressive sequence from a deep shelf-slope environment during the Wuchiapingian Stage to a slope-basin setting during the Changhsingian. The Wuchiapingian–Changhsingian boundary is located within the Black Stripe Formation (Beauchamp et al., 2009). The formation stratigraphically consists of dark grey to black chert and black siliceous shale. Upper Permian conodonts are rare in the Sverdrup Basin and strong provincialism exists because of large latitudinal gradients in water temperature (Mei and Henderson, 2001). Nonetheless, correlation with tropical regions can still be made by the occurrence of *Mesogondolella rosenkrantzi*, possibly associated with *M. sheni,* that suggests a Late Permian age for the Black Stripe Formation (Mei and Henderson, 2001). The $\delta^{13}C_{org}$ profile for this interval also displays two negative shifts of ~2 ‰ that bracket the WCB within the basal part of the Black Stripe Formation (Beauchamp et al., 2009) (Fig. 2).

Previous work has shown that the $\delta^{13}C_{org}$ record of the Sverdrup Basin closely matches global organic and inorganic carbon isotope records and can be easily correlated (Grasby et al., 2013).

3. Methods

Samples (n = 24) from the Lianyuan section were collected from 0 to 15 m (Fig. 2) for both organic carbon isotope ($\delta^{13}C_{org}$) and rhenium-osmium (Re-Os) analysis. Samples for the Meishan, Shangsi, and Buchanan Lake sections were only collected for Re-Os analysis using archived sample material from previous studies. For the Meishan section, samples (n = 16) from 12 m below to 8 m above the WCB were obtained from archived drill core that had been utilised for $\delta^{13}C_{carb}$ isotope analysis (Cao et al., 2009). For the Shangsi section, the only remaining archived outcrop samples (n = 16; Shen et al., 2013) were obtained from 9 m above to 11 m below the WCB. Lastly, for the Buchanan Lake section, sub-samples (n = 16) from 75 m to 105 m collected during a prior $\delta^{13}C_{org}$ study (Beauchamp et al., 2009) were used.

3.1 Re–Os analysis

Before crushing, all samples (20–70 g) were polished to eliminate contamination from cutting and drilling marks. The samples were then air dried at 60 °C for ~12 hours, and broken into chips with no metal contact. Samples were crushed to a fine powder (~30 μm) in a Zirconia ceramic dish using a shatterbox. The sample analytical protocol and Re–Os isotope analysis were carried out at the Durham Geochemistry Centre (Laboratory for Sulfide and Source Rock Geochronology and Geochemistry, and Arthur Holmes Laboratory) at Durham University. For sample digestion, a Cr^{VI}–H_2SO_4 solution was employed to preferentially liberate hydrogenous Re and Os from the organic matter, limiting any contamination from Re and Os in the detritus (Selby and Creaser, 2003). Sample powder weights of ~0.3 to 1 g with a known amount of ^{190}Os and ^{185}Re tracer (spike) solution and 8 mL of 0.25 g/g Cr^{VI}-H_2SO_4 solution were reacted in a sealed carius tube for 48 h at 220 °C (Selby and Creaser, 2003). Osmium was purified using solvent extraction ($CHCl_3$), micro-distillation and anion chromatography methods. From

the osmium extracted solution, rhenium was isolated using solvent extraction ($NaOH\text{-}C_3H_6O$) and then purified by anion chromatography. The isolated Re and Os fractions were loaded onto Ni and Pt filaments, respectively. Isotopic measurements were determined using a ThermoElectron TRITON mass spectrometer with static Faraday collection for Re and secondary electron multiplier in peak-hopping mode for Os. Total procedural blanks during this study were 12.5 ± 4.5 pg and 0.12 ± 0.06 pg (1σ S.D., n = 3) for Re and Os, respectively, with an average $^{187}Os/^{188}Os$ value of 0.34 ± 0.20 (n = 3). The initial $^{187}Os/^{188}Os$ values were calculated using the equation:

$$^{187}Os/^{188}Os_{initial} = {}^{187}Os/^{188}Os_{measured} - (^{187}Re/^{188}Os_{measured}*(EXP(\lambda * t)-1))$$

Where λ is ^{187}Re decay constant $1.666e^{-11}a^{-1}$ (Smoliar et al., 1996) and t is the depositional age. The Permian timescale of China constrains the WCB at 254.14 Ma (Shen et al., 2019b). This age is in agreement with that constrained by U-Pb zircon ages from the studied sections and the available biostratigraphy (Fig. 2). In this study, Os_i values are calculated using a modelled stratigraphic age for each sample interval based on the U-Pb zircon geochronology and a constant sedimentation rate. For the Shangsi section, the sedimentation rate is determined using the two U-Pb zircon ages and applied to the whole section. Likewise, for the Meishan section, the sedimentation rate is calculated using the available U-Pb zircon ages and the age of CIE1 (254.3 Ma) based on the U-Pb zircon dates from the Shangsi section. For the Buchanan Lake and Lianyuan sections, the sedimentation rates are determined assuming the CIE1 to be 254.3 Ma and CIE2 to be 253.6 Ma based on the U-Pb zircon geochronology of the Meishan and Shangsi sections. Detailed results are presented in the supplementary tables.

3.2 Organic carbon isotope analysis

Organic carbon isotopic data were established for the Lianyuan section at the Stable Isotope Laboratory at Northwestern University. Prior to analysis, samples were acidified: ~1 g of powder was mixed with 15 mL 2 N HCl and left for 24 hours. Acid was decanted and then

214 the samples were repeatedly rinsed with Milli-Q water until acid was neutralised. Samples were
215 then dried down in an oven at 50 ˚C for 2-3 days until samples are completely dry. The samples
216 were ground to fine powder and loaded into tin capsules. Carbon isotope values ($\delta^{13}C_{org}$) were
217 analysed using a Costech ECS4010 Elemental Analyser coupled to a Thermo Delta V Plus
218 isotope ratio mass spectrometer. To correct for instrument mass fractionation and adjust to the
219 VPBD per mil scale, raw results were calibrated using acetanilide and urea (Indiana University
220 - IU) standards (Schimmelmann et al., 2009). The average precision (1s) on IU-acetanilide
221 standards throughout the analytical run was ±0.09 ‰ (n = 10), and the range of precision on
222 sample duplicates (n = 3) is (±0.14 to ±0.26 ‰, mean ±0.21 ‰).

223 **4. Results**

224 **4.1 Carbon isotope profile**

225 The $\delta^{13}C_{org}$ data established for the Lianyuan section from this study yield values
226 ranging from -22 to -26 ‰ (Fig. 2; Table S1). The $\delta^{13}C_{org}$ values show a steady decline from -
227 22 to -24 ‰ in the Upper Lungtan to Lower Talung Formations, with a one-point excursion to
228 -25 ‰ at 4.5 m below the WCB. From here the $\delta^{13}C_{org}$ values return to ~-23 ‰ and remain
229 relatively stable until the WCB. At 2 m above the WCB the $\delta^{13}C_{org}$ values exhibit a sharp
230 negative excursion to -26 ‰, and then return to less negative values (~24 ‰).

231 The $\delta^{13}C_{org}$ profile of the Lianyuan section is similar to carbon isotope profiles for the
232 Meishan, Shangsi, and Buchanan Lake sections (Fig. 2; Beauchamp et al., 2009; Shen et al.,
233 2013), which we also briefly describe below. At the Meishan section, the $\delta^{13}C_{carb}$ profile for
234 this interval exhibits two negative shifts (2 – 3 ‰). Within the Upper Wuchiapingian Lungtan
235 Formation $\delta^{13}C_{carb}$ shifts from ~0 to -2 ‰, and then to ~4 ‰. Remaining at ~4 ‰, $\delta^{13}C_{carb}$
236 shows a 3 ‰ negative excursion within the basal part of the Changhsingian Stage in the
237 Changhsing Formation, and then returns to values of ~3 ‰. At Shangsi, the $\delta^{13}C_{carb}$ profile

238 shows a steady trend to more negative values through the Talung Formation, to a nadir of -3 ‰
239 just below the WCB, which is followed by a trend to 1.5 ‰ at the WCB. The $\delta^{13}C_{carb}$ values
240 then remain similar until a ~3 ‰ negative excursion within the basal part of Changhsingian
241 Stage. At Buchanan Lake, the $\delta^{13}C_{org}$ profile for this interval exhibits two negative shifts. The
242 $\delta^{13}C_{org}$ values decrease from ~ -26 ‰ to -27 ‰ at the basal part of the Black Stripe Formation,
243 which then return to the pre-excursion values around the WCB. Above the WCB, $\delta^{13}C_{org}$ values
244 decline to ~ -27 ‰ and then increase to ~ -26 ‰.
245
246 **4.2 Rhenium and osmium abundance and $^{187}Os/^{188}Os$ isotope stratigraphy**
247 At the Lianyuan section, Re and Os abundances range from 0.15 to 30.63 ppb and 18.4
248 to 296.1 ppt (^{192}Os = ~10 – 95 ppt) (Table S1). The Os_i in the Lungtan Formation is radiogenic
249 (1.2) and becomes gradually unradiogenic to a nadir of 0.20 (coinciding with the lower $\delta^{13}C_{org}$
250 negative excursion) within the coal interval of the Talung Formation. The Os_i values then
251 increase steadily to ~0.5 at ~2 m below the WCB, then decline steadily to ~0.16 within the
252 basal Changhsingian (overlapping with the upper $\delta^{13}C_{org}$ negative excursion), and finally return
253 to more radiogenic Os_i values of ~0.5 coincident with $\delta^{13}C_{org}$ returning to more stable values.
254 Changes in the common Os budget, represented by ^{192}Os, broadly follow that shown by Os_i
255 (Fig. 2). For example, in the basal part of the Lungtan Formation ^{192}Os increases dramatically
256 to ~95 ppt (coeval with the decline in Os_i) and then declines gradually to ~40 ppt (where Os_i
257 increases to ~0.5), and again increases to the base of the WCB (where Os_i trends to more non-
258 radiogenic). Within the basal Changhsingian ^{192}Os is relatively constant at ~10 ppt.
259 At the Meishan section, Re and Os values range from 1.35 to 131.02 ppb and 22.2 to
260 887.5 ppt, respectively (^{192}Os = ~11 to 200 ppt) (Table S2). In contrast to Lianyuan, there is no
261 apparent relationship between ^{192}Os and Os_i (Fig. 2). The ^{192}Os abundance is predominantly
262 ~11 ppt, with higher abundances within the Lungtan Formation at ~50 m (up to 186 ppt), and

263 then within the basal Changhsingian within the lower Changhsing Formation (up to 207 ppt).
264 The Os_i in the basal part of the Lungtan Formation is ~0.6-0.5 and then abruptly drops to an
265 unradiogenic value of ~0.2 close to the top of the Lungtan Formation, coincident with the lower
266 $\delta^{13}C_{carb}$ excursion (Fig. 2). The Os_i values then gradually shift to more radiogenic (~0.8) at ~0.5
267 m below the WCB, and then decline to ~0.4 at the base of the Changhsing Formation,
268 coincident with the upper $\delta^{13}C_{carb}$ excursion. The Os_i then returns to more radiogenic values of
269 ~0.5.

270 At the Shangsi section, Re and Os range from 0.78 to 1017.76 ppb and 10.9 to 3932.2
271 ppt, respectively (^{192}Os = ~3.5 – 483.6 ppt) (Table S3). Like the Meishan section, no apparent
272 relationship between ^{192}Os and Os_i is observed (Fig. 2). The Os_i values through the Late
273 Wuchiapingian, prior to the lower $\delta^{13}C_{carb}$ excursion, are similar within uncertainty (~0.5). In
274 contrast to the other sections coincident with the lower $\delta^{13}C_{carb}$ excursion, Os_i becomes slightly
275 more radiogenic (~0.70), and then exhibits a single-point shift to less radiogenic values (~0.35)
276 within the basal Changhsingian, which then abruptly returns to more radiogenic values of ~0.5
277 and remains relatively similar stratigraphically through the second carbon isotope excursion
278 (Fig. 2).

279 At the Buchanan Lake section, Re and Os abundances range from 0.11 to 25.91 ppb
280 and 72.9 to 240.9 ppt, respectively (^{192}Os = ~38 to 73 ppt) (Table S4). The Os_i values in the
281 basal part of the Black Stripe Formation (Upper Wuchiapingian) are relatively invariant (~0.55),
282 and specifically show no change in composition within the lower $\delta^{13}C_{org}$ negative excursion,
283 as was observed for the Shangsi section. In contrast, and coincident with the upper $\delta^{13}C_{org}$
284 negative excursion, Os_i values decrease relatively sharply to ~0.33 during the earliest
285 Changhsingian and then increase to pre-excursion values of up to ~0.80.

286 **5. Discussion**

5.1 Seawater Os_i during Late Wuchiapingian

For the Shangsi and Buchanan Lake sections, trends to less radiogenic Os_i only coincide within the temporal period associated with the second carbon isotope excursion observed within the Early Changhsingian (Fig. 2). In contrast, the Os_i trends toward less radiogenic values in the Lianyuan and Meishan sections, although of different magnitude, are coincident with both carbon isotope profile excursions, and are thus considered time-correlative (Fig. 2).

The Meishan, Shangsi, and Buchanan Lake sections are interpreted to represent deposition in a more distal marine setting (e.g., shallow marine, slope-shelf, and open marine; Jin et al., 2006b; Shen et al., 2013; Beauchamp et al., 2009). As such, the moderately radiogenic Os_i values (~0.5–0.6) for the majority of the measured stratigraphic interval for the Meishan, Shangsi, and Buchanan Lake sections potentially suggest the Os_i value is a more global representation of the ocean $^{187}Os/^{188}Os$ composition. In contrast, the Os_i values in the Late Wuchiapingian of the Lungtan Formation of the Lianyuan section are much more radiogenic (~1.20) than those from the same time interval in the Meishan (~0.60), Shangsi (~0.55) and Buchanan Lake (~0.55) sites. The highly radiogenic Os_i values of Lianyuan are attributed to the dominant delivery of weathered crustal materials in response to the more proximal depositional setting (e.g., deltaic plain; Wang and Jin, 2000) that the Lianyuan section strata record.

5.2 Unradiogenic Os_i excursions and the link with volcanism

The first unradiogenic Os_i shift, which is only observed in the Lianyuan and Meishan sections, occurred concurrently with a sea-level rise event (Li and Shen, 2008; Wang and Jin, 2000). If this unradiogenic shift were caused simply by a shift in the local water column to more fully marine conditions, an Os_i value intermediate between contemporaneous seawater Os_i and local radiogenic Os_i values would be expected. However, the Os_i at Lianyuan (~0.2) and Meishan (~0.17) is more non-radiogenic than that of open marine seawater (~0.55), as

inferred from the open marine sections of Shangsi and Buchanan Lake. We conclude that the shift to non-radiogenic Os_i reveals an actual perturbation in the seawater Os reservoir within the Paleo-Tethys Ocean, but not the entire Paleo-Tethys and the global Panthalassa Ocean. The absence of any change to more non-radiogenic Os_i for the more open marine setting represented by the Shangsi section, where Os_i becomes slightly more radiogenic (Fig. 2), suggests that the $^{187}Os/^{188}Os$ of the Paleo-Tethys Ocean is controlled by the site's palaeogeographic setting. As such, the mechanism driving the change in the seawater $^{187}Os/^{188}Os$ composition observed at Lianyuan and Meishan was only capable of affecting the more proximal depositional settings.

The observed non-radiogenic Os_i shifts may be caused by (1) reduced radiogenic Os input from weathered continental material, (2) increased non-radiogenic Os flux from enhanced hydrothermal activity and/or meteorite impact events, or (3) the Os isotope composition of weathered material being less radiogenic due to erosion of different hinterland strata (Peucker-Ehrenbrink and Ravizza, 2000). Climatic cooling is capable of diminishing the weathering rate of ancient crust. Given the extent of the non-radiogenic Os_i shifts (~0.16 and 0.20 at Lianyuan), a nearly complete shutdown of the weathering process (e.g., due to glaciation) would be required to cause the magnitude of the observed non-radiogenic Os_i shift (Finlay et al., 2010). It has been argued that the Permian climate experienced a cooling during the earliest Wuchiapingian in response to weathering of the Emeishan continental flood basalts (Yang et al., 2018). Cooling based on oxygen isotope proxies has also been invoked for the Changhsingian, however it is unclear whether this cooling was due to glaciation (Chen et al., 2013). The termination age of the youngest known Permian glaciation (P4) is 254.5 Ma (Metcalfe et al., 2015). Given the timing of the known P4 glaciation and uncertainty in the extent of climate cooling, a cooling event is unlikely to be the mechanism causing the non-radiogenic Os_i shifts observed across the WCB.

No extraterrestrial impact event is known to be associated with the WCB, therefore we attribute the source of non-radiogenic Os to magmatic activity and the associated weathering of newly erupted/fresh basaltic units. Two large igneous provinces (LIPs) are known in the Middle and Late Permian: the Emeishan and the Siberian Traps LIPs. Even though dating results have linked the Emeishan LIP with the end-Guadalupian mass extinction (Zhong et al., 2014; Bond et al., 2015; Wignall et al., 2009; Grasby et al., 2015), and the Siberian Traps LIP with the end-Permian mass extinction (Burgess et al., 2014, 2017; Saunders and Reichow, 2009), the age of the Emeishan LIP does overlap, in part, with the Wuchiapingian–Changhsingian boundary age (254.14 Ma; Shen et al., 2019b). However, it is not certain if the magmatism at the WCB, as suggested here, is associated with the Emeishan LIP (based on available data). Although the first non-radiogenic pulse is only recorded in the Lianyuan and Meishan sections, the second is detected in all four sections. The difference in magnitude of the two negative Os_i excursions may suggest that the second pulse of volcanism was more intense and had a more significant global impact on the $^{187}Os/^{188}Os$ composition of the ocean.

The Os_i values in the Lianyuan section recover to more radiogenic levels following the excursions to non-radiogenic Os_i values. Yet, the Os_i values at Lianyuan are significantly more non-radiogenic than the Os_i values for correlated stratigraphic intervals recorded for the more open marine sites observed at Meishan, Shangsi, and Buchanan Lake. The long-lasting non-radiogenic Os_i signature in the Lianyuan section likely suggests that the Lianyuan section remained relatively restricted, or in a proximal depositional setting, following the marine transgression. It is probable that Os in the local water mass at Lianyuan was dominated by non-radiogenic Os input from the weathering of fresh mafic igneous rocks or continued mafic volcanism.

5.3 LIP events and mass extinction

Magmatism associated with LIP's is often implicated in rapid environmental destabilization and severe biological crises, such as the Siberian Traps LIP and end-Permian mass extinction, Emeishan volcanism and the end-Guadalupian mass extinction, Decan Traps and the end-Cretaceous mass extinction, North Atlantic Igneous Province and the Palaeocene –Eocene Thermal Maximum, Karoo-Ferrar Traps and the Early Jurassic ocean anoxic event, etc. (Bond and Grasby, 2017; Courtillot and Renne, 2003; Wignall, 2001). Nonetheless, not all LIP events have driven environmental change and mass extinction (Wignall, 2001). Several factors may affect the impact of LIP magmatism. The emplacement style of the LIP (i.e., vertical or lateral; intrusive or extrusive) appears to play a critical role in determining the magnitude of environmental impact (Burgess et al., 2017; Renne et al., 2015). A recent study of the end-Permian mass extinction and Siberian LIP suggests that catastrophic global environmental change is more likely caused by sill complexes rather than flood basalts and/or dike components (Burgess et al., 2017). The composition of the strata into which sills are intruded also plays an important role on volatile generation (Burgess et al., 2017). Further, a small volume volcanic eruption may not have a notable effect on global Earth systems. Moreover, a large volume eruption over a long period may also have less effect than a small but rapid eruption (Renne et al., 2015). As there was no discernible mass extinction event associated with WCB volcanism, it was likely associated with a small-volume eruption. Even if it was a LIP, it might have erupted through volatile-poor substrates. Thus, generation of only a limited amount of climate-altering volatiles may have permitted the biosphere to overcome the effects of volcanic gas emission. As such, WCB volcanism may have only had a regional impact, with any climate perturbation rapidly overturned back to pre-eruption-like conditions.

5.4 WCB carbon isotope excursions

Two pulses of carbon isotope excursion are detected in both carbonate and organic carbon isotope records. The excursions of carbonate carbon isotope values have a (slightly)

385 larger magnitude than those of the organic carbon isotope records. The cause(s) of the WCB
386 carbon isotope excursions remain unclear. Previous research has suggested a reduction of
387 primary production based on the correlation between total organic carbon (TOC) and $\delta^{13}C_{org}$
388 (Wei et al., 2015). However, sea level fall is also considered to have exposed coal/peat
389 formations that released ^{12}C enriched CO_2 through the weathering of organic matter (Shao et
390 al., 2010). Enhanced continental weathering should increase radiogenic Os input to the ocean
391 and thus lead to an increase in the Os_i values, which is apparent in our data. Further, there is
392 no regression documented around the WCB. In contrast, a regional transgression is documented
393 in South China (Li and Shen, 2008; Wang and Jin, 2000). Previously, the role of volcanic
394 outgassing was ruled out as no such event was known for this time interval (Wei et al., 2015).
395 But our new Os_i data, which is consistent with increased volcanism, suggests that atmospheric
396 input of isotopically light carbon may have contributed to the negative CIEs spanning the WCB.
397 This would be similar to the even larger CIEs associated with the Siberian Trap Eruptions of
398 the Late Permian and Early Triassic (Payne and Kump, 2007). Such volcanism may also have
399 disturbed the environment sufficiently to cause decreases in primary production (Wei et al.,
400 2015). The first pulse of volcanism during the Late Wuchiapingian was probably regional in
401 scale, and only perturbed local $^{187}Os/^{188}Os$ in South China, but was capable of affecting the
402 global carbon cycle. In contrast, the second pulse of volcanism during the Late Changhsingian
403 may have been more intense and affected both the global carbon and seawater $^{187}Os/^{188}Os$
404 record.

405 **6. Conclusion**

406 The first shift to non-radiogenic Os_i during the latest Wuchiapingian is only detected at
407 two sections in South China (Lianyuan and Meishan), whereas the second excursion to non-
408 radiogenic Os_i values during the earliest Changhsingian is observed in all four studied sections.
409 The two excursions to unradiogenic Os_i correlate with two negative carbon isotope excursions

across the WCB interval. The Os_i shifts are interpreted to reflect volcanic events, with only the Early Changhsingian event perturbing the global ocean $^{187}Os/^{188}Os$ ratio. Volcanism has long been proposed as a killing mechanism associated with mass extinctions. The volcanism associated with the WCB, however, appears to have been insufficient to drive massive environmental change to disrupt the biosphere. The injection of isotopically light carbon from volcanic outgassing may have been an additional mechanism that caused the CIEs across the WCB. This study demonstrates how Os geochemistry may be used to assess the relative magnitude of ancient volcanic events, which are proving to be one of the most common drivers of major biogeochemical perturbations in Earth history.

Acknowledgements

We thank Chuanbo Shen and Tingting Lei for assistance with field work. This work was supported by the Strategic Priority Research Program (B) of CAS (XDB26000000, XDB18000000). For technical support we thank Antonia Hoffman, Geoff Nowell and Chris Ottley. We gratefully acknowledge the TOTAL Endowment Fund and the CUG Wuhan Dida Scholarship to DS, and the University of Durham and China Scholarship Council to ZL.

Data Availability

Datasets related to this article can be found at http://XXXX, an open-source online data repository hosted at Mendeley Data (Liu et al., 2019).

References

Bagherpour, B., Bucher, H., Schneebeli-Hermann, E., Vennemann, T., Chiaradia, M., Shen, S.-z., 2018. Early Late Permian coupled carbon and strontium isotope chemostratigraphy from South China: Extended Emeishan volcanism? Gondwana Research 58, 58-70.

433 Bai, X., Luo, G., Wu, X., Wang, Y., Huang, J., Wang, X., 2008. Carbon Isotope Records
434 Indicative of Paleoceanographical Events at the Latest Permian Dalong Formation at
435 Shangsi, Northeast Sichuan, China. Journal of China University of Geosciences 19,
436 481-487.
437 Beauchamp, B., Henderson, C.M., Grasby, S.E., Gates, L.T., Beatty, T.W., Utting, J., James,
438 N.P., 2009. Late Permian Sedimentation in the Sverdrup Basin, Canadian Arctic: The
439 Lindstrom and Black Stripe Formations. Bulletin of Canadian Petroleum Geology 57,
440 167-191.
441 Bond, D.P.G., Grasby, S.E., 2017. On the causes of mass extinctions. Palaeogeography,
442 Palaeoclimatology, Palaeoecology 478, 3-29.
443 Bond, D. P. G., Savov, I., Wignall, P. B., Joachimski, M. M., Sun, Y., Grasby, S. E.,
444 Beauchamp, B., Blomeier, D. P. G., 2015. An abrupt extinction in the Middle Permian
445 (Capitanian) of the Boreal Realm (Spitsbergen) and its link to anoxia and acidification.
446 GSA Bulletin 127, 1411-1421.
447 Burgess, S.D., Bowring, S., Shen, S.-z., 2014. High-precision timeline for Earth's most severe
448 extinction. Proceedings of the National Academy of Sciences 111, 3316-3321.
449 Burgess, S.D., Bowring, S.A., 2015. High-precision geochronology confirms voluminous
450 magmatism before, during, and after Earth's most severe extinction. Science Advances,
451 1(7).
452 Burgess, S.D., Muirhead, J.D., Bowring, S.A., 2017. Initial pulse of Siberian Traps sills as the
453 trigger of the end-Permian mass extinction. Nature Communications 8, 164.
454 Cao, C., Love, G.D., Hays, L.E., Wang, W., Shen, S., Summons, R.E., 2009. Biogeochemical
455 evidence for euxinic oceans and ecological disturbance presaging the end-Permian
456 mass extinction event. Earth and Planetary Science Letters 281, 188-201.

457 Chen, B., Joachimski, M.M., Shen, S.-z., Lambert, L.L., Lai, X.-l., Wang, X.-d., Chen, J., Yuan,
458 D.-x., 2013. Permian ice volume and palaeoclimate history: Oxygen isotope proxies
459 revisited. Gondwana Research 24, 77-89.
460 Courtillot, V.E., Renne, P.R., 2003. On the ages of flood basalt events. Comptes Rendus
461 Geoscience 335, 113-140.
462 Erwin, D.H., 2006. Extinction: How Life on Earth Nearly Ended 250 Million Years Ago.
463 Princeton University Press, Princeton.
464 Finlay, A.J., Selby, D., Gröcke, D.R., 2010. Tracking the Hirnantian glaciation using Os
465 isotopes. Earth and Planetary Science Letters 293, 339-348.
466 Grasby, S. E., Beauchamp, B., Bond, D. P. G., Wignall, P. B., Sanei, H., 2015, Mercury
467 anomalies associated with three extinction events (Capitanian Crisis, Latest Permian
468 Extinction and the Smithian/Spathian Extinction) in NW Pangea. Geological Magazine
469 153, 285-297.
470 Grasby, S. E., Beauchamp, B., Embry, A. F., Sanei, H., 2013. Recurrent Early Triassic ocean
471 anoxia. Geology41,175-178.
472 Grasby, S. E., Beauchamp, B., 2008. Intrabasin variability of the carbon-isotope record across
473 the Permian-Triassic transition, Sverdrup Basin, Arctic Canada. Chemical Geology 253,
474 141-150.
475 Jin, Y., Shen, S., Henderson, C.M., Wang, X., Wang, W., Wang, Y., Cao, C., Shang, Q., 2006a.
476 The Global Stratotype Section and Point (GSSP) for the boundary between the
477 Capitanian and Wuchiapingian Stage (Permian). Episodes 29, 253-262.
478 Jin, Y., Wang, Y., Henderson, C., Wardlaw, B.R., Shen, S., Cao, C., 2006b. The Global
479 Boundary Stratotype Section and Point (GSSP) for the base of Changhsingian Stage
480 (Upper Permian). Episodes 29, 175-182.

481 Korte, C., Kozur, H.W., 2010. Carbon-isotope stratigraphy across the Permian–Triassic
482 boundary: A review. Journal of Asian Earth Sciences 39, 215-235.
483 Kump, L.R., Arthur, M.A., 1999. Interpreting carbon-isotope excursions: carbonates and
484 organic matter. Chemical Geology 161, 181-198.
485 Li, W.-Z., Shen, S.-Z., 2008. Lopingian (Late Permian) brachiopods around the
486 Wuchiapingian-Changhsingian boundary at the Meishan Sections C and D, Changxing,
487 South China. Geobios 41, 307-320.
488 Liu, X.-c., Wang, W., Shen, S.-z., Gorgij, M.N., Ye, F.-c., Zhang, Y.-c., Furuyama, S., Kano,
489 A., Chen, X.-z., 2013. Late Guadalupian to Lopingian (Permian) carbon and strontium
490 isotopic chemostratigraphy in the Abadeh section, central Iran. Gondwana Research 24,
491 222-232.
492 Mei, S., Henderson, C.M., 2001. Evolution of Permian conodont provincialism and its
493 significance in global correlation and paleoclimate implication. Palaeogeography,
494 Palaeoclimatology, Palaeoecology 170, 237-260.
495 Metcalfe, I., Crowley, J.L., Nicoll, R.S., Schmitz, M., 2015. High-precision U-Pb CA-TIMS
496 calibration of Middle Permian to Lower Triassic sequences, mass extinction and
497 extreme climate-change in eastern Australian Gondwana. Gondwana Research 28, 61-
498 81.
499 Payne, J.L., Kump, L.R., 2007. Evidence for recurrent Early Triassic massive volcanism from
500 quantitative interpretation of carbon isotope fluctuations. Earth and Planetary Science
501 Letters 256, 264-277.
502 Peucker-Ehrenbrink, B., Ravizza, G., 2000. The marine osmium isotope record. Terra Nova 12,
503 205-219.

504 Renne, P.R., Sprain, C.J., Richards, M.A., Self, S., Vanderkluysen, L., Pande, K., 2015. State
505 shift in Deccan volcanism at the Cretaceous-Paleogene boundary, possibly induced by
506 impact. Science 350, 76-78.
507 Riccardi, A., Kump, L.R., Arthur, M.A., D'Hondt, S., 2007. Carbon isotopic evidence for
508 chemocline upward excursions during the end-Permian event. Palaeogeography,
509 Palaeoclimatology, Palaeoecology 248, 73-81.
510 Saunders, A., Reichow, M., 2009. The Siberian Traps and the End-Permian mass extinction: a
511 critical review. Chinese Science Bulletin 54, 20-37.
512 Schimmelmann, A., Albertino, A., Sauer, P.E., Qi, H., Molinie, R., Mesnard, F., 2009. Nicotine,
513 acetanilide and urea multi-level ^{2}H-, ^{13}C- and ^{15}N-abundance reference materials for
514 continuous-flow isotope ratio mass spectrometry. Rapid Communications in Mass
515 Spectrometry 23, 3513-3521.
516 Selby, D., Creaser, R.A., 2003. Re–Os geochronology of organic rich sediments: an evaluation
517 of organic matter analysis methods. Chemical Geology 200, 225-240.
518 Shao, L., Zhang, P., Dou, J., Shen, S., 2000. Carbon isotope compositions of the Late Permian
519 carbonate rocks in southern China: their variations between the Wujiaping and
520 Changxing formations. Palaeogeography, Palaeoclimatology, Palaeoecology 161, 179-
521 192.
522 Shellnutt, J.G., 2014. The Emeishan large igneous province: A synthesis. Geoscience Frontiers
523 5, 369-394.
524 Shen, S.-z., Cao, C.-q., Zhang, H., Bowring, S.A., Henderson, C.M., Payne, J.L., Davydov,
525 V.I., Chen, B., Yuan, D.-x., Zhang, Y.-c., Wang, W., Zheng, Q.-f., 2013. High-
526 resolution δ13Ccarb chemostratigraphy from latest Guadalupian through earliest
527 Triassic in South China and Iran. Earth and Planetary Science Letters 375, 156-165.

528 Shen, S.-z., Crowley, J.L., Wang, Y., Bowring, S.A., Erwin, D.H., Sadler, P.M., Cao, C.-q.,
529 Rothman, D.H., Henderson, C.M., Ramezani, J., Zhang, H., Shen, Y., Wang, X.-d.,
530 Wang, W., Mu, L., Li, W.-z., Tang, Y.-g., Liu, X.-l., Liu, L.-j., Zeng, Y., Jiang, Y.-f.,
531 Jin, Y.-g., 2011. Calibrating the End-Permian Mass Extinction. Science 334, 1367-1372.
532 Shen, S.-Z., Henderson, C.M., Bowring, S.A., Cao, C.-Q., Wang, Y., Wang, W., Zhang, H.,
533 Zhang, Y.-C., Mu, L., 2010. High-resolution Lopingian (Late Permian) timescale of
534 South China. Geological Journal 45, 122-134.
535 Shen, S., Ramezani, J., Chen, J., Cao, C., Erwin, D., Zhang, H., Xiang, L., Schoepfer, S.,
536 Henderson, C., Zheng, Q., A. Bowring, S., Wang, Y., Li, X.-H., Wang, X.-D., Yuan,
537 D., Zhang, Y., Lin, M., Wang, J., Wu, Y.S., 2019a. A sudden end-Permian mass
538 extinction in South China. Geological Society of America Bulletin 131, 205-223.
539 Shen, S., Zhang, H., Zhang, Y., Yuan, D., Chen, B., He, W., Mu, L., Lin, W., Wang, W., Chen,
540 J., Wu, Q., Cao, C., Wang, Y., Wang, X., 2019b. Permian integrative stratigraphy and
541 timescale of China. Science China: Earth Sciences 62, 154-188.
542 Smoliar, M.I., Walker, R.J., Morgan, J.W., 1996. Re-Os ages of group IIA, IIIA, IVA, and IVB
543 iron meteorites. Science 271, 1099.
544 Svensen, H., Planke, S., Polozov, A.G., Schmidbauer, N., Corfu, F., Podladchikov, Y.Y.,
545 Jamtveit, B., 2009. Siberian gas venting and the end-Permian environmental crisis.
546 Earth and Planetary Science Letters 277, 490-500.
547 Wang, W., Cao, C., Wang, Y., 2004. The carbon isotope excursion on GSSP candidate section
548 of Lopingian–Guadalupian boundary. Earth and Planetary Science Letters 220, 57-67.
549 Wang, Y., Jin, Y., 2000. Permian palaeogeographic evolution of the Jiangnan Basin, South
550 China. Palaeogeography, Palaeoclimatology, Palaeoecology 160, 35-44.
551 Wei, H., Yu, H., Wang, J., Qiu, Z., Xiang, L., Shi, G., 2015. Carbon isotopic shift and its cause
552 at the Wuchiapingian–Changhsingian boundary in the Upper Permian at the Zhaojiaba

section, South China: Evidences from multiple geochemical proxies. Journal of Asian Earth Sciences 105, 270-285.

Wignall, P.B., 2001. Large igneous provinces and mass extinctions. Earth-Science Reviews 53, 1-33.

Wignall, P.B., Sun, Y., Bond, D.P.G., Izon, G., Newton, R.J., Védrine, S., Widdowson, M., Ali, J.R., Lai, X., Jiang, H., Cope, H., Bottrell, S.H., 2009. Volcanism, Mass Extinction, and Carbon Isotope Fluctuations in the Middle Permian of China. Science 324, 1179-1182.

Yang, J., Cawood, P.A., Du, Y., Condon, D.J., Yan, J., Liu, J., Huang, Y., Yuan, D., 2018. Early Wuchiapingian cooling linked to Emeishan basaltic weathering? Earth and Planetary Science Letters 492, 102-111.

Ye, Q., Jiang H., 2016. Conodont Biostratigraphy and a Negative Excursion in Carbonate Carbon Isotopes across the Wuchiapingian–Changhsingian Boundary at the Dawoling Section，Hunan Province. Earth Science 41, 1883-1892. (in Chinese)

Yuan, D.-X., Shen, S.-z., Henderson, C.M., Chen, J., Zhang, H., Zheng, Q.-f., Wu, H., 2019. Integrative timescale for the Lopingian (Late Permian): A review and update from Shangsi, South China. Earth-Science Reviews 188, 190-209.

Zhong, Y.-T., He, B., Mundil, R., Xu, Y.-G., 2014. CA-TIMS zircon U–Pb dating of felsic ignimbrite from the Binchuan section: Implications for the termination age of Emeishan large igneous province. Lithos 204, 14-19.

Ziegler, A.M., Hulver, M.L., Rowley, D.B., 1997. Permian world topography and climate. In: Martini, I.P. (Ed.), Late Glacial and Postglacial Environmental Changes–Quaternary, Carboniferous–Permian and Proterozoic. Oxford University Press, New York, pp. 111–146.

List of Figures:

578 **Figure 1.** Late Permian paleogeographic maps showing the studied areas. (A) Changhsingian
579 global paleogeographic reconstruction map showing the position of the studied sections; base
580 map after Ziegler et al. (1997). (B) South China: 1, Meishan; 2, Shangsi; 3, Lianyuan; base
581 map modified from Wang and Jin (2000). White circles represent other Wuchiapingian–
582 Changhsingian boundary sections where negative carbon isotope excursions are detected:
583 Canada Arctic: (a) Buchanan Lake; Iran: (b) Kuh-e-Ali Bashi, (c) Abadeh; South China: (d)
584 Zhaojiaba, (e) Dukou, (f), Wenjiangsi, (g) Matan, (h) Dawoling.

585 **Figure 2.** Carbon isotope (black), Os_i (red) and ^{192}Os (blue) stratigraphy. The $\delta^{13}C_{carb}$ data of
586 Meishan and Shangsi are from Shen et al. (2013). Conodont zones for South China sections
587 are from Shen et al. (2013b). The U-Pb zircon ages are from Shen et al. (2011). The $\delta^{13}C_{org}$
588 data of Lianyuan are from this study. The $\delta^{13}C_{org}$ and conodont data of the Buchanan Lake
589 section are from Beauchamp et al. (2009) and Mei and Henderson (2001). The purple vertical
590 bars represent the background seawater Os_i values (~0.5 - 0.6). See text for discussion. Ages
591 of the Emeishan and Siberian volcanism are from Shellnutt (2014) and Burgess and Bowring
592 (2015). Glaciation termination age is from Metcalfe et al. (2015).

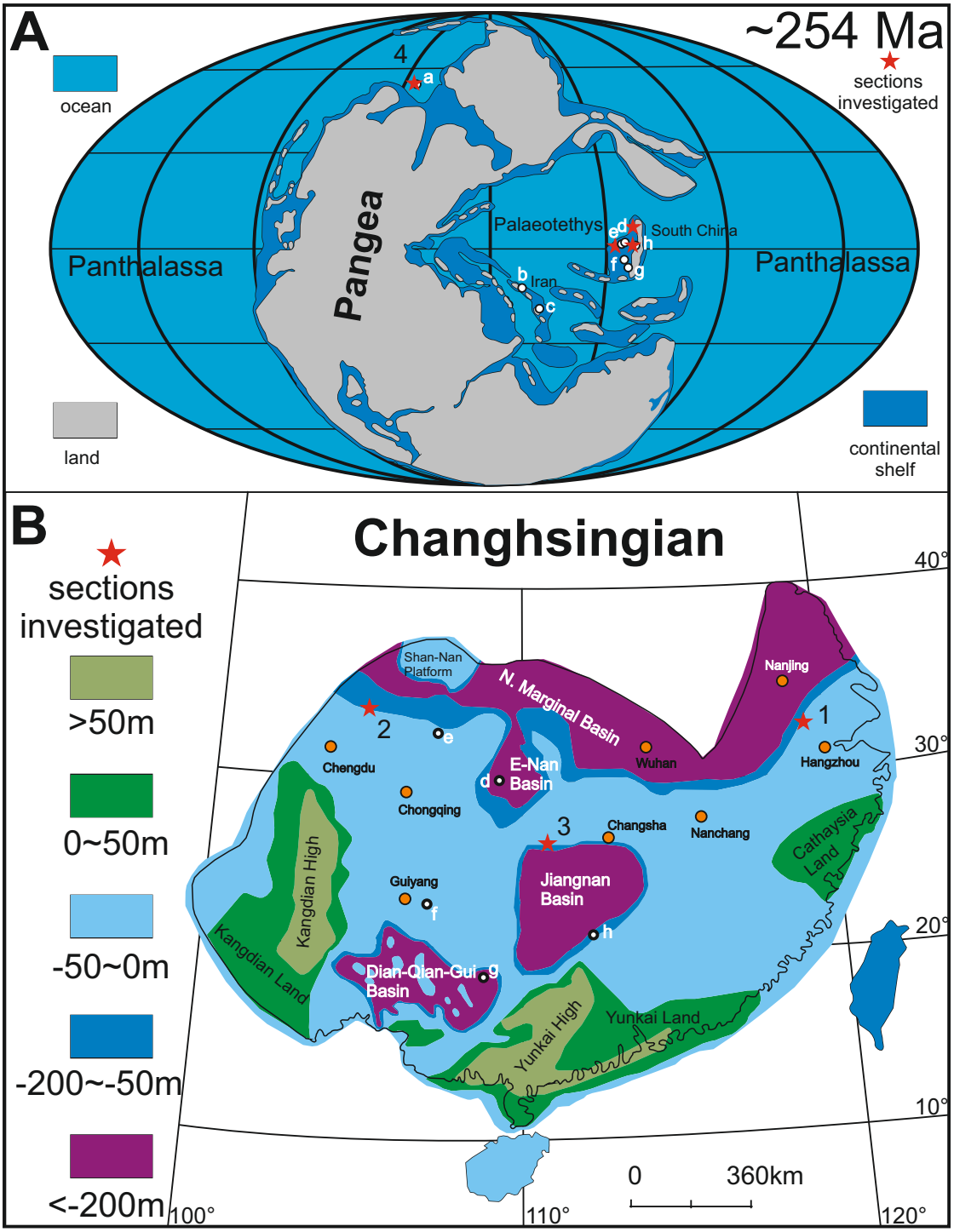
A
~254 Ma
sections investigated
ocean
land
continental shelf
Pangea
Panthalassa
Panthalassa
Palaeotethys
South China
Iran
4
a
b
c
d
e
f
g
h
B
Changhsingian
sections investigated
>50m
0~50m
-50~0m
-200~-50m
<-200m
Shan-Nan Platform
N. Marginal Basin
E-Nan Basin
Jiangnan Basin
Dian-Qian-Gui Basin
Kangdian Land
Kangdian High
Yunkai High
Yunkai Land
Cathaysia Land
Nanjing
Wuhan
Hangzhou
Chengdu
Chongqing
Changsha
Nanchang
Guiyang
1
2
3
40°
30°
20°
10°
100°
110°
120°
0
360km

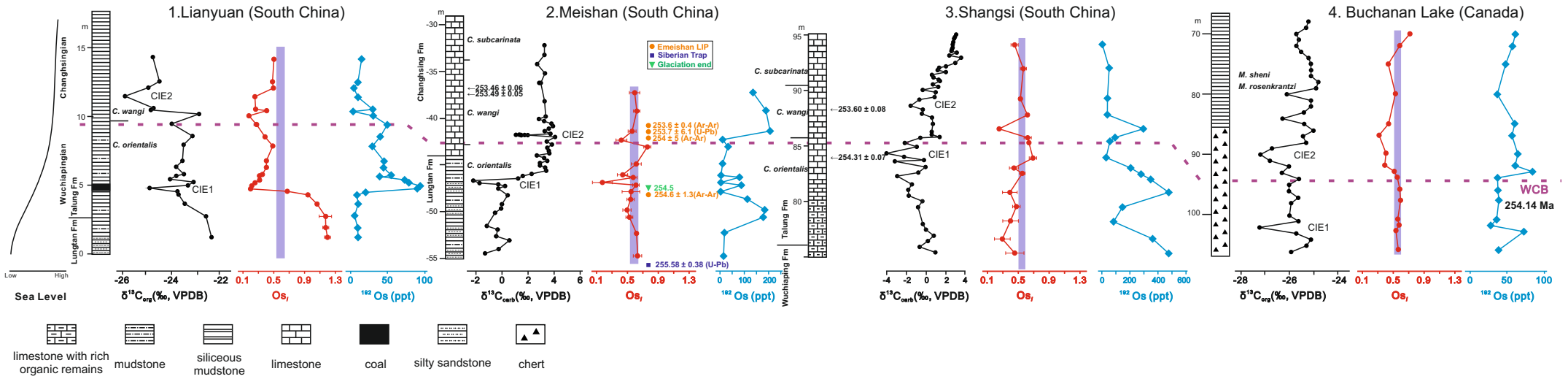
1.Lianyuan (South China)
2.Meishan (South China)
3.Shangsi (South China)
4. Buchanan Lake (Canada)
Changhsingian
Wuchiapingian
Talung Fm
Lungtan Fm
Changhsing Fm
Wuchiaping Fm
C. wangi
C. orientalis
C. subcarinata
CIE1
CIE2
Emeishan LIP
Siberian Trap
Glaciation end
253.46 ± 0.06
253.49 ± 0.05
253.6 ± 0.4 (Ar-Ar)
253.7 ± 6.1 (U-Pb)
254 ± 5 (Ar-Ar)
254.5
254.6 ± 1.3(Ar-Ar)
255.58 ± 0.38 (U-Pb)
253.60 ± 0.08
254.31 ± 0.07
M. sheni
M. rosenkrantzi
WCB
254.14 Ma
Low
High
Sea Level
δ13Corg(‰, VPDB)
δ13Ccarb(‰, VPDB)
Osi
182 Os (ppt)
limestone with rich organic remains
mudstone
siliceous mudstone
limestone
coal
silty sandstone
chert

Table S1. Re-Os and $\delta^{13}C_{org}$ data for Lianyuan section.

Depth (m)	Re (ppb)	±	Os (ppt)	±	^{192}Os (ppt)	±	^{187}Re/^{188}Os	±	^{187}Os/^{188}Os	±	rho	Os_i	±	$\delta^{13}C_{org}$(VPDB)	Age (Ma)
12.7	11.72	0.03	70.9	0.7	15.7	0.1	1489.8	13.4	6.8	0.1	0.875	0.50	0.003	-24.7	253.30
11.2	8.10	0.02	46.4	0.5	9.8	0.1	1639.8	22.0	7.4	0.1	0.923	0.48	0.004	-24.5	253.48
10.8	3.23	0.01	20.9	0.3	4.8	0.1	1325.8	35.2	6.1	0.2	0.942	0.50	0.009	-24.9	253.53
10.2	8.46	0.02	47.2	0.5	10.0	0.1	1679.9	21.9	7.4	0.1	0.930	0.25	0.002	-25.9	253.60
9.4	30.63	0.07	155.9	1.2	30.2	0.2	2020.2	11.8	8.8	0.1	0.756	0.26	0.001	-24.7	253.69
9.3	3.31	0.01	19.0	0.4	4.1	0.1	1617.2	50.2	7.3	0.2	0.957	0.41	0.009	-24.8	253.71
9.0	27.22	0.07	148.2	1.7	31.1	0.4	1741.7	24.2	7.5	0.1	0.936	0.17	0.002	-22.9	253.74
8.4	29.74	0.08	202.1	1.8	49.7	0.5	1189.7	11.2	5.3	0.1	0.867	0.28	0.002	-24.0	253.81
7.6	6.71	0.02	120.5	0.7	41.0	0.3	325.8	2.1	1.8	0.0	0.684	0.38	0.002	-23.1	253.91
7.0	6.99	0.02	93.7	0.6	29.6	0.2	470.0	3.4	2.5	0.0	0.725	0.49	0.003	-23.5	253.98
6.0	6.76	0.02	132.2	0.8	45.5	0.3	295.6	1.9	1.7	0.0	0.681	0.41	0.002	-23.5	254.10
5.6	6.56	0.02	128.7	0.7	44.3	0.3	295.0	1.9	1.7	0.0	0.682	0.41	0.002	-23.8	254.14
5.1	5.78	0.02	152.3	0.8	54.9	0.3	209.5	1.3	1.2	0.0	0.649	0.35	0.002	-23.5	254.20
5	3.34	0.01	106.8	0.7	39.4	0.3	168.4	1.5	1.0	0.0	0.685	0.32	0.002	-23.8	254.22
4.8	10.18	0.03	209.1	1.0	73.3	0.3	276.4	1.4	1.5	0.0	0.638	0.31	0.001	-24.0	254.24
4.6	16.49	0.04	237.0	1.2	78.4	0.3	418.2	2.0	2.0	0.0	0.627	0.25	0.001	-23.1	254.26
4.4	24.52	0.06	296.1	1.7	94.1	0.4	518.3	2.7	2.4	0.0	0.670	0.22	0.001	-23.3	254.29
4.2	10.54	0.03	248.8	1.5	90.2	0.7	232.5	1.8	1.2	0.0	0.693	0.20	0.001	-24.9	254.31
4	1.96	0.01	58.2	0.6	20.4	0.3	191.4	3.0	1.5	0.0	0.711	0.67	0.009	-23.7	254.33
3.8	0.55	0.01	25.5	0.6	9.0	0.4	121.7	5.3	1.5	0.1	0.702	0.95	0.035	-23.7	254.36
3.2	0.34	0.01	29.4	0.6	10.5	0.4	63.8	2.9	1.3	0.1	0.662	1.06	0.039	-23.4	254.43
2.4	0.15	0.01	18.4	0.7	6.5	0.5	46.9	4.3	1.4	0.2	0.648	1.17	0.086	-22.6	254.52
1.7	0.23	0.01	28.8	0.6	10.3	0.4	43.7	2.2	1.4	0.1	0.609	1.18	0.045	-22.1	254.61
1.0	0.23	0.01	29.9	0.6	10.6	0.4	42.7	2.1	1.4	0.1	0.609	1.21	0.046	-22.3	254.69

All uncertainties are given at 2σ level.

Os_i values are determined using an estimated stratigraphic age model.

Rho is the associated error correlation.

Table S2. Re and Os data for Meishan section.

Depth (m)	Re (ppb)	±	Os (ppt)	±	^{192}Os (ppt)	±	^{187}Re/^{188}Os	±
-37.29	115.73	0.29	657.8	4.5	136.3	0.5	1689.7	7.3
-39.22	94.15	0.23	737.1	4.6	188.6	0.7	993.0	4.3
-41.41	131.02	0.32	877.5	5.7	206.7	0.7	1261.3	5.5
-42.39	7.69	0.02	51.5	0.4	12.3	0.1	1240.0	7.5
-43.10	18.04	0.05	143.1	0.9	36.2	0.1	990.4	4.6
-44.94	5.96	0.02	48.4	0.4	12.6	0.1	938.8	7.0
-46.19	2.37	0.01	22.2	0.2	6.3	0.1	747.7	7.0
-46.41	44.92	0.14	325.2	2.1	80.2	0.3	1114.6	5.4
-46.95	4.56	0.01	26.8	0.3	6.0	0.1	1510.9	14.2
-47.24	44.75	0.11	346.7	2.2	88.3	0.3	1008.2	4.5
-47.97	3.68	0.01	24.9	0.2	5.9	0.1	1239.6	11.9
-48.80	67.94	0.17	474.6	3.0	114.9	0.4	1176.4	5.0
-49.90	124.66	0.31	804.7	5.2	185.8	0.7	1334.6	5.7
-50.65	95.57	0.24	710.8	4.5	178.8	0.6	1063.5	4.6
-52.39	4.67	0.01	66.8	0.5	21.1	0.1	441.5	3.1
-54.87	1.35	0.00	40.9	0.5	14.5	0.3	185.1	3.8

All uncertainties are given at 2σ level.

Os_i values are determined using an estimated stratigraphic age model.

Rho is the associated error correlation.

$^{187}Os/^{188}Os$	±	rho	Os_i	±	Age (Ma)
7.7	0.04	0.584	0.59	0.07	253.48
4.8	0.03	0.571	0.62	0.04	253.55
5.9	0.03	0.580	0.56	0.05	253.60
5.7	0.04	0.697	0.42	0.07	253.73
5.0	0.03	0.596	0.76	0.05	253.82
4.6	0.04	0.632	0.61	0.07	254.05
3.6	0.04	0.769	0.44	0.07	254.21
5.3	0.03	0.554	0.57	0.05	254.24
6.6	0.07	0.791	0.17	0.13	254.31
4.9	0.03	0.598	0.61	0.04	254.35
5.8	0.07	0.787	0.54	0.12	254.44
5.5	0.03	0.569	0.54	0.05	254.55
6.2	0.03	0.579	0.49	0.05	254.69
5.0	0.03	0.576	0.52	0.05	254.78
2.5	0.02	0.661	0.62	0.04	255.01
1.4	0.04	0.704	0.63	0.06	255.33

Table S3. Re-Os data for Shangsi section.

Depth (m)	Re (ppb)	±	Os (ppt)	±	^{192}Os (ppt)	±	^{187}Re/^{188}Os	±	^{187}Os/^{188}Os	±	rho	Os_i	±	Age (Ma)
94.3	0.78	0.00	10.9	0.1	3.5	0.1	442.2	6.6	2.32	0.04	0.818	0.45	0.05	252.74
92.1	21.15	0.06	190.1	1.2	52.2	0.2	805.5	3.7	3.98	0.02	0.561	0.57	0.04	253.07
89.4	20.00	0.05	153.0	1.0	39.1	0.2	1017.7	4.8	4.84	0.03	0.605	0.54	0.03	253.48
87.9	18.74	0.05	153.5	1.0	40.2	0.2	928.2	4.4	4.56	0.03	0.611	0.63	0.03	253.72
86.7	120.26	0.31	1051.2	6.1	296.8	1.0	805.9	3.5	3.67	0.02	0.540	0.25	0.03	253.91
85.8	79.12	0.20	459.2	3.2	96.3	0.3	1635.1	7.2	7.56	0.04	0.585	0.62	0.05	254.04
85.5	23.61	0.06	213.3	1.3	58.2	0.2	807.6	3.5	4.07	0.02	0.579	0.64	0.04	254.09
84.1	16.77	0.04	130.8	0.9	33.1	0.1	1009.1	4.8	4.98	0.03	0.590	0.69	0.05	254.31
83.1	153.59	0.38	933.0	6.2	207.5	0.7	1472.6	6.3	6.69	0.03	0.580	0.44	0.06	254.46
82.6	124.07	0.30	1060.9	6.3	285.3	1.0	865.2	3.8	4.23	0.02	0.580	0.55	0.04	254.53
80.9	841.76	2.06	3460.3	26.5	483.6	1.7	3462.5	14.5	15.11	0.07	0.570	0.38	0.10	254.80
79.6	122.20	0.30	699.6	4.9	147.2	0.5	1651.4	7.2	7.50	0.04	0.583	0.47	0.05	255.00
78.3	146.66	0.36	603.3	4.8	84.1	0.3	3471.3	15.7	15.18	0.08	0.616	0.39	0.10	255.20
76.7	678.04	1.68	2722.8	21.7	366.3	1.3	3682.3	15.8	15.99	0.08	0.564	0.28	0.11	255.44
75.4	1017.76	2.48	3932.2	31.2	476.3	1.6	4250.8	17.8	18.59	0.09	0.567	0.45	0.12	255.65

All uncertainties are given at 2σ level.

Os_i values are determined using an estimated stratigraphic age model.

Rho is the associated error correlation.

Table S4. Re-Os data for Buchanan Lake section.

Depth (m)	Re (ppb)	±	Os (ppt)	±	^{192}Os (ppt)	±	^{187}Re/^{188}Os	±
-70	25.912	0.063	230.6	1.4	61.9	0.2	832.4	3.7
-72	6.331	0.016	164.0	0.9	57.4	0.3	219.6	1.3
-75	2.841	0.007	129.3	0.8	48.3	0.4	117.1	1.1
-80	0.761	0.003	95.7	1.0	36.7	0.7	41.2	0.9
-85	1.707	0.005	158.6	1.3	61.1	0.8	55.6	0.8
-87	0.136	0.002	142.4	2.6	57.1	2.3	4.7	0.2
-90	1.859	0.005	168.1	1.3	65.0	0.9	56.9	0.8
-92	0.597	0.003	153.8	2.9	60.8	2.4	19.5	0.8
-93	9.343	0.023	240.9	1.3	84.9	0.5	219.0	1.3
-94	0.282	0.002	96.8	0.8	37.6	0.5	14.9	0.2
-96	1.005	0.003	100.4	1.1	38.1	0.8	52.5	1.1
-98	0.945	0.003	106.4	1.2	40.4	0.8	46.5	1.0
-101	0.141	0.002	94.3	1.8	36.7	1.5	7.6	0.3
-102	0.109	0.002	73.0	1.4	28.4	1.1	7.6	0.3
-103	10.152	0.025	213.3	1.1	73.0	0.3	276.5	1.5
-106	1.215	0.004	101.8	0.9	38.5	0.5	62.8	0.9

All uncertainties are given at 2σ level.

Os_i values are determined using an estimated stratigraphic age model.

Rho is the associated error correlation.

$^{187}Os/^{188}Os$	±	rho	Os_i	±	Age (Ma)
4.25	0.02	0.592	0.74	0.03	252.51
1.51	0.01	0.630	0.59	0.01	252.62
0.94	0.01	0.680	0.44	0.01	252.78
0.70	0.02	0.697	0.53	0.02	253.05
0.68	0.01	0.694	0.44	0.01	253.33
0.35	0.02	0.663	0.33	0.02	253.44
0.65	0.01	0.694	0.41	0.01	253.60
0.47	0.03	0.703	0.39	0.03	253.71
1.44	0.01	0.631	0.52	0.01	253.76
0.62	0.01	0.620	0.56	0.01	253.82
0.81	0.02	0.699	0.58	0.02	253.93
0.79	0.02	0.698	0.59	0.02	254.04
0.59	0.03	0.666	0.56	0.03	254.20
0.60	0.03	0.641	0.57	0.03	254.26
1.70	0.01	0.623	0.53	0.01	254.31
0.83	0.02	0.692	0.56	0.02	254.47